Development of ultrafine grained Al 7075 by cryogenic temperature large strain extrusion machining

Xiaolong Yin, Yunyun Pi, Di He,[b] Jiayang Zhang, and Wenjun Deng[a]
School of Mechanical and Automotive Engineering, South China University of Technology, Guangzhou 510641, China

(Received 5 April 2018; accepted 14 August 2018)

Large strain extrusion machining (LSEM) emerges as an innovative severe plastic deformation method of fabricating ultrafine grained materials. However, substantial heat generated during LSEM would sacrifice the mechanical properties of materials. Cryogenic temperature (CT) LSEM is put forward to overcome this shortcoming. The Al 7075 was processed by cryogenic and room temperature (RT) LSEM to investigate their comparative effects on mechanical and microstructural properties. Results indicate that the chip morphology of CT LSEM is featured with better integrity. Grains are refined to less than 200 nm by CT LSEM. A more complicated microstructure with high dislocation density is observed in the CT LSEM specimens. The hardness of cryogenic and RT LSEM specimens increases with the compression ratio and reaches the highest values of 187HV and 170HV, respectively. Dislocation strengthening is the main contributor, accounting for the higher hardness of CT LSEM specimens.

I. INTRODUCTION

The Al 7××× series alloys have extensively been applied in automobile and aerospace structures and other high strength components owing to their high strength-to-weight ratio, and high thermal and electrical conductivity.[1–3] It is well known that refining the grain structure to ultrafine grained (UFG) regime can further enhance the mechanical properties of these Al alloys. Consequently, preparation of UFG Al alloys has raised increasing attention recently. Severe plastic deformation (SPD) is the most frequently used technique for the production of UFG materials. However, preparation of UFG Al 7×××× alloys with conventional SPD methods requires large plastic strains and exhibits limited success by virtue of the formation of metastable precipitates that restrict the formability of the alloys during processing at room temperature (RT).[4] One alternative way to increase the deformability is increasing the process temperature, and homogeneous structures can be produced. However, elevated temperature will probably give rise to over-aging and dynamic recovery, thus sacrificing the mechanical properties of the alloys.[5,6] Furthermore, large amounts of heat generated during the SPD process at RT will also exert negative impact on the material. To obviate this difficulty, deformation at cryogenic temperature (CT) has been identified as a promising route of producing UFG Al alloys and eliminating the temperature-induced effects simultaneously.

To date, cryogenic SPD methods are widely used to achieve UFG materials in various pure metal and alloys. Li et al.[7] studied the microstructure refinement mechanics of pure Cu with dynamic plastic deformation and found that high density of deformation twins induced by CTs plays a critical role in formation of nanosized precipitates. Zhao et al.[8] proposed a new strategy for simultaneously improving the ductility and the yield strength of nanostructured Al alloys through cryogenic rolling followed by low temperature aging. Fritsch et al.[5] imposed high strains on the difficult-to-work Al 7075 using cryogenic ECAP and gained UFG alloys with increased ductility and improved workability. Yu et al.[9] used cryogenic roll bonding to fabricate Al/Ti/Al laminate sheets. Then, they found that edge cracks occurred in laminate sheets created by RT bonding while they failed to appear when subjected to cryogenic roll bonding.

Among these SPD techniques, large strain extrusion machining (LSEM), an attractive method, is capable of imposing large strains on materials in a single pass while overcoming the limitations of conventional SPD methods.[10] However, the side effect of temperature is inevitable, the same in LSEM due to the generation of heat created by plastic work and friction. To overcome this shortcoming, in this paper, cryogenic temperature large strain extrusion machining (CT-LSEM), which combines the advantages of LSEM and cryogenic approach, was put forward for the first time. As shown in Fig. 1, LSEM is an alteration of conventional machining by applying a constraining tool across from the cutting tool to form an

[a]Address all correspondence to this author.
e-mail: dengwj@scut.edu.cn
[b]This article has been updated since original publication. A notice detailing this change has also been published at https://doi.org/10.1557/jmr.2018.383.
DOI: 10.1557/jmr.2018.313

 © Materials Research Society 2018

https://doi.org/10.1557/jmr.2018.313 Published online by Cambridge University Press

extrusion channel, in which chip formation is regarded as a plain-strain process, when t_d, t_{ch}, α, and V represent the uncut chip thickness, chip thickness, rake angle, and machining velocity, respectively. The workpiece moves in the direction perpendicular to the cutting edge with a speed of V, thus forcing the material to enter the extrusion channel to acquire a geometrically controllable chip, as illustrated in Fig. 1. The ratio of t_{ch} and t_d is defined as the compression ratio λ:

$$\lambda = t_{ch}/t_d \quad . \tag{1}$$

The shear strain imposed in the chip is calculated by

$$\varepsilon = \frac{\lambda}{\cos\alpha} + \frac{1}{\lambda\cos\alpha} - 2\tan\alpha \quad . \tag{2}$$

Considerable research related to LSEM has been accomplished in the last decade. Deng et al.[11,12] systematically studied the influence of the rake angle and the chip compression ratio on the deformation behaviors and material properties in LSEM with finite element modeling (FEM) and experimental methods. Then, Rao et al.[13] adopted LSEM to produce fine-grained continuous Ti–6Al–4V foils with suppressed shear localization by suitable altering texture of Ti–6Al–4V. Iglesias et al.[14] investigated the wear resistance behaviors of three kinds of nanostructured OFHC copper created by LSEM and also found that the wear resistance was direction-dependent. Efe et al.[15] used upper bound, slip line field, and heat source models to analyze the mechanics of the deformation field in LSEM and successfully prepared UFG microstructures of poor workability materials via controlling the hydrostatic pressure and temperature in the deformation zone.

To the best of our knowledge, there is no relevant literature on the characterization of UFG Al alloys produced by LSEM in the cryogenic environment. In this paper, the solution-treated (ST) Al 7075 was processed by CT-LSEM with different compression ratios. Room-temperature large strain extrusion machining (RT-LSEM) was also conducted for comparison. The machining process and material properties were characterized by employing FEM, hardness measurements, optical microscopy (OM), and transmission electron microscopy (TEM). The main concerns of this paper include (i) developing a new strategy to prepare UFG alloys with enhanced mechanical properties; (ii) exploring the relationships between hardness and microstructure of the LSEM specimens; and (iii) revealing the effect of processing temperature on the machining results.

II. METHODOLOGY

A. Experimental details

Figure 2 shows the setup and associated parameters of LSEM, in which different values of λ can be realized by changing t_{ch} and t_d through adjusting shims. Three screws are set to ensure the smooth operation of LSEM. The commercial Al 7075 circular tube with the outer diameter of 70 mm and the thickness of 6 mm was served as the model material. The chemical composition of this alloy is 5.60 Zn, 2.50 Mg, 1.60 Cu, 0.50 Fe, 0.40 Si, 0.30 Mn, 0.23 Cr, 0.20 Ti, and Al balance. A slot was machined in the end of the workpiece to keep the machining process working well, as presented in Fig. 2.

The workpiece was ST at 470 °C for 2.5 h and then quenched in water. Before CT-LSEM, the ST material was first immersed into liquid nitrogen with a duration of at least 20 min to reach a steady state. Then, the CT-LSEM process was immediately implemented to avert the temperature rise. During CT-LSEM, the workpiece was dipped into liquid nitrogen for few minutes prior to the next pass. The machining conditions used in

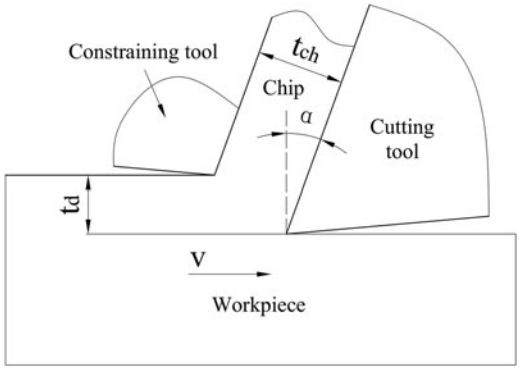


FIG. 1. Schematic view of LSEM, the material undergoes extrusion and shear simultaneously when it enters into the extrusion channel formed by the cutting tool and the constraining tool, obtaining a shape-controlled chip. The chip thickness t_{ch} is determined a prior unlike the conventional machining in which the chip is formed naturally.

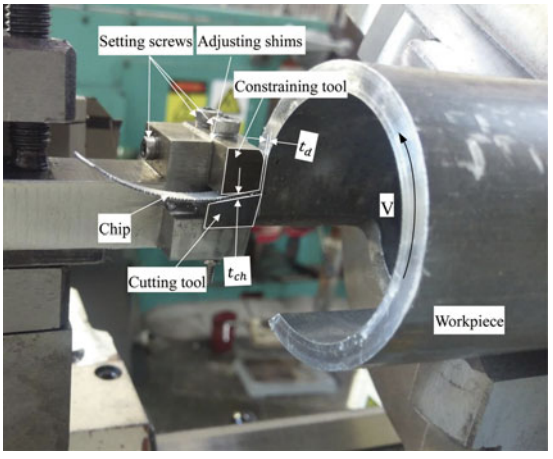


FIG. 2. Photographic view of the setup for LSEM and associated geometric parameters.

https://doi.org/10.1557/jmr.2018.313 Published online by Cambridge University Press

the experiments are as follows: the uncut chip thickness t_d, the rake angle α, and the cutting velocity V were set as 0.5 mm, 20°, and 92 mm/s, respectively, while the compression ratio λ varied with three values, namely 1.4, 1.6, and 1.8, by altering the chip thickness t_{ch} to 0.7 mm, 0.8 mm, and 0.9 mm through adjusting shims mounted on the tools. For each λ, at least three experiments were repeated to reduce the experimental errors. RT-LSEM was also performed for comparison.

Microhardness tests were conducted on the plane parallel to the tool rake face with a load of 50 g for 15 s. At least 20 readings were taken to calculate the average hardness of each sample. The microstructure features of the alloys were acquired by adopting OM. For this purpose, the samples were mechanically polished with abrasive paper of 600, 800, 1200, 1500, and 2000 grit in sequence, followed by fine polishing with the diamond paste of 1 μm to the mirror finish. Grinding of the chips was started from the surface coming in contact with the tool rake face. Keller's reagent (95 mL H_2O, 2.5 mL HNO_3, 1.5 mL HCl, and 1.0 mL HF) was adopted to etch the specimens. The dislocation network and the microstructure of specimens were characterized by TEM using the FEI Tecani F20 (FEI, Hillsboro, Oregon) equipment that operates at an accelerating voltage of 200 kV. For TEM characterization, foils with the thickness of about 1 mm were cut from the center of the cross section of each specimen, which was parallel to the extrusion direction. The foils were mechanically ground to the thickness of about 50 μm. Then discs with the diameter of 3 mm were punched from the foils, and they were first twin jet eletropolished (10 vol% $HClO_4$ in ethanol, 20 V, −25 °C) and then polished with an argon ion beam.

B. FEM details

FEM is adopted to simulate machining with great success. Significant parameters of machining, such as, cutting forces, chip morphology, temperatures, strains, and strain rates, can be well predicted and calculated by FEM prior to any machining that is performed. Accordingly, FEM has advantages in reducing the manufacturing cost and saving the processing time over the trial and error approaches.[16] For LSEM, unreasonable cutting conditions will lead to the failure of experiments or even the destruction of the apparatus. Therefore, the FEM simulations have been conducted in advance to determine the suitable parameters. In this paper, a commercial FEM code DEFORM 2D, based on the updated Lagrangian formulation, is used to simulate the LSEM processes. Chip separation from the workpiece is realized by adopting continuous remeshing technique. Figure 3 shows the mesh and boundary conditions for LSEM, in which meshes in front of the cutting tool tip are of local high density to simulate chip formation accurately and catch the larger

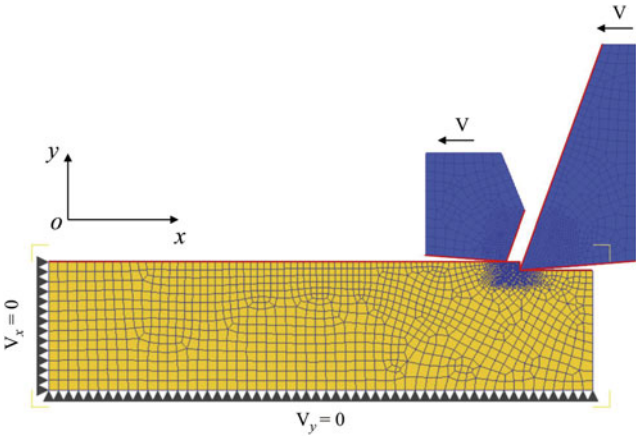


FIG. 3. Mesh and boundary condition settings for LSEM. During LSEM, the workpiece is maintained stationary while the tools move at a speed of V, the top sides of the workpiece and the lower-left sides of the cutting tool and the lower-right sides of the constraining tool are set as heat exchange boundaries between the workpiece and the tools.

deformation in the machining process. The object types of the tools are regarded rigidly, and the workpiece is plastic.

During machining, the bottom and left boundaries of the workpiece are fixed in y and x directions, respectively, and the tools move along the $-x$ direction at a certain velocity. The LSEM parameters used in FEM are consistent with the experimental conditions. The contact boundaries between the tools and the workpiece enable heat to exchange mutually, while the rest boundaries are able to exchange heat with the environment. In the machining process, the heat transferred by radiation is negligible. Therefore, the emissivity is set zero for all conditions.[6] To simulate the CT-LSEM process as exactly as possible, the heat constants of materials in the cutting zone such as environment temperature and convection coefficient are set to be consistent with the cryogenic condition.

A constitutive equation, which is the most versatile format in flow stress models, is implemented in the FE code to model the material behaviors. The equation is defined as follows:

$$f(\sigma) = \sigma(\varepsilon, \dot{\varepsilon}, T) \quad , \tag{3}$$

where σ is the equivalent flow stress; ε is the effective plastic strain; $\dot{\varepsilon}$ is the effective strain rate; and T is the temperature. As the cutting velocity is extremely low (92 mm/s), the interface between the chip and the tool is governed by the sliding condition.[17] The Coulomb criterion is therefore used as the friction model, which is defined as follows:

$$f_s = \mu p \quad , \tag{4}$$

where f_s is the friction stress; μ is the friction coefficient; p is the interface pressure between the chip and the tool. In this study, the same friction coefficient 0.4 through experiments and calculation is used for all conditions.

https://doi.org/10.1557/jmr.2018.313 Published online by Cambridge University Press

III. RESULTS AND DISCUSSION

A. Chip morphology

The combined effects of workpiece material properties and machining conditions are main factors that determine chip morphology.[18] In this research, the processing temperature is the only variable that distinguish CT-LSEM and RT-LSEM. Accordingly, it is meaningful to understand the effects of temperature on the chip morphology. Figure 4 shows the chip morphology differences between RT-LSEM and CT-LSEM, in which chips of the former are segmented whereas the latter are continuous. In the upper surfaces of RT-LSEM chips, cracks appear and propagate until the chips fracture. By contrast, the upper surfaces of CT-LSEM chips are relatively smooth with only few tiny cracks occurring near the edges of the chip. Obviously, the chip morphology of LSEM is temperature dependent, and CT promotes the workability of this alloy because the fracture strain increases with the reduction of deformation temperature and the ductility of Al alloys at CT is higher than that at RT.[9] In fact, the ductility has a proportional relationship with the work-hardening capacity.[19] Work hardening is attributed to the generation and accumulation of dislocations, which results in pileups at the grain boundaries during deformation. Therefore, the ductility of the alloy is higher due to the increased dislocation accumulation ability by suppressing the dynamic recovery at CT.

Furthermore, Al alloys are kinds of face-centered cubic (fcc) structures with a lot of slip systems, and multiple slip systems are prone to appearing at low temperatures, which makes the alloys difficult to fracture. The ductile–brittle transition of the alloys will not occur even at CT. This result is opposite to what is commonly known, or in other words, the result is adverse to the situation that brittle fractures are likely to occur for most metal when the temperature decreases. In addition, as the temperature decreases, Al alloys can absorb more energy. As a result, the fracture of the material is delayed.[20]

Figure 5 shows the predicted temperature distributions of RT-LSEM and CT-LSEM for a selected λ. Higher temperatures are concentrated in the region of the chip root where the adiabatic shear occurs for RT-LSEM. As for CT-LSEM, temperature values decrease sharply compared with RT-LSEM. It is also interesting to note that a large gap appears between the chip and the constraining tool as shown in Fig. 5(a), while the chip in Fig. 5(b) is highly filled in the extrusion channel. The reason for this phenomenon is

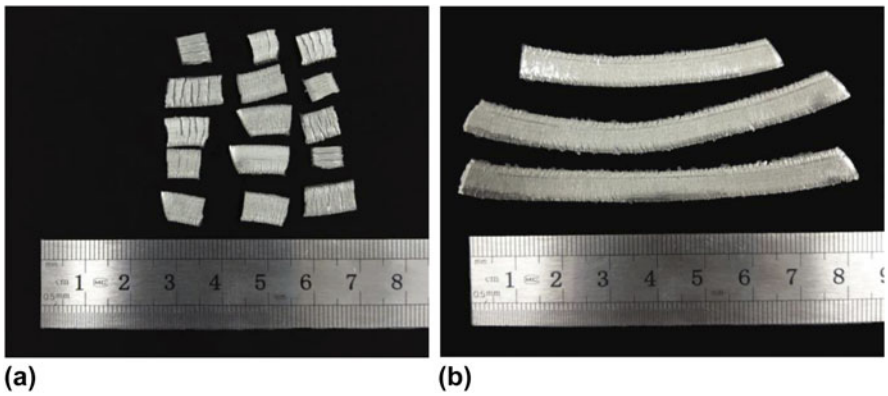


FIG. 4. Chip morphology difference created by (a) RT-LSEM and (b) CT-LSEM with the compression ratio of λ = 1.8.

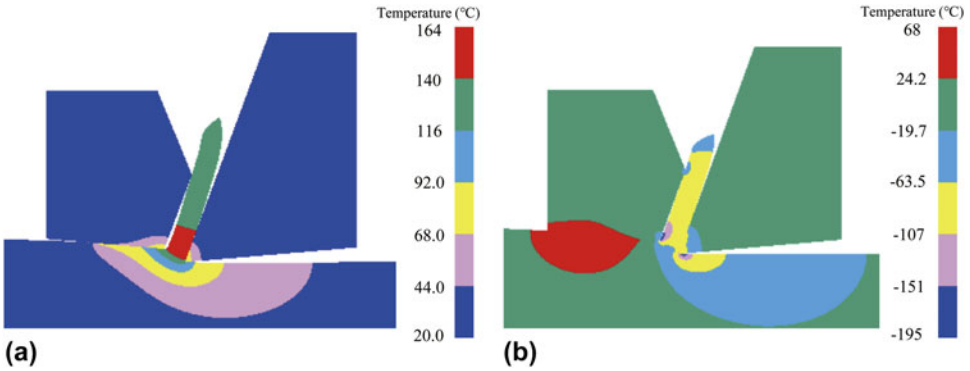


FIG. 5. Predicted temperature distributions of (a) RT-LSEM and (b) CT-LSEM with the compression ratio of λ = 1.8.

https://doi.org/10.1557/jmr.2018.313 Published online by Cambridge University Press

that the width of the extrusion channel for $\lambda = 1.8$ exceeds the upper limit[21] that the chip can reach at RT. In summary, deformation at the cryogenic regime results in high dislocation density by suppressing the dynamic recovery process and retains the solutes in the ST alloys, all of which will lead to an increase of work-hardening ability and the suppression of strain localization and crack formation.[3,5,22] Therefore, CT-LSEM possesses an advantage over RT-LSEM in guaranteeing the integrity of the chips.

B. Microstructure

OM images of the starting material (solution-treated Al 7075) and specimens subjected to CT-LSEM and RT-LSEM are illustrated in Fig. 6. As can be seen in Fig. 6(e), the grain size of the starting material is in the range of 10–40 μm, and subgrains of less than 5 μm can be observed in the microstructure. After being processed by LSEM, both materials exhibit a homogeneous microstructure as shown in Figs. 6(a)–6(d). The microstructures are highly refined with grains and grain boundaries

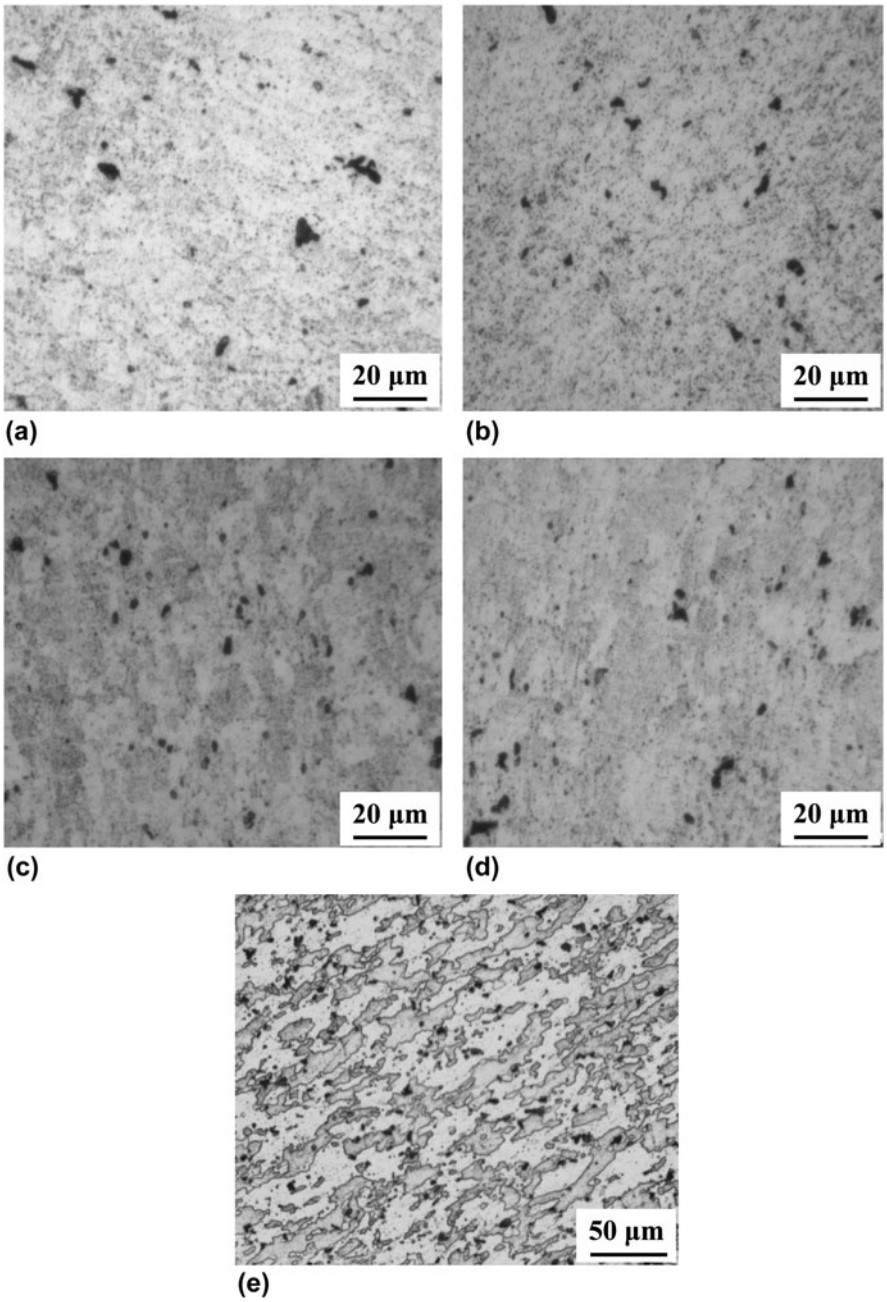


FIG. 6. OM images of the (a) RT-LSEM and (b) CT-LSEM samples for $\lambda = 1.4$; (c) RT-LSEM and (d) CT-LSEM samples for $\lambda = 1.8$, (e) as the solution-treated Al 7075 alloy (the starting material).

https://doi.org/10.1557/jmr.2018.313 Published online by Cambridge University Press

being hard to discern. To obtain more detailed information on microstructure features, the TEM technique is indispensable.

Figure 7 shows TEM micrographs of the samples processed by RT-LSEM and CT-LSEM for compression ratios of 1.4 and 1.8, respectively. It is obvious to note that the grain size of samples subjected to LSEM for $\lambda = 1.4$ is larger than that for $\lambda = 1.8$, which indicates that the degree of grain refinement increases with strains. Then the phenonmenon is consistent with the observations in previous research.[11] Some better distinguished grains are equiaxed with the grain size of about 200 nm and extremely small subgrains can be observed in the CT-LSEM sample for $\lambda = 1.4$. The rest regions are diffused when grain boundaries are ill-defined. The microstructure of the CT-LSEM sample for $\lambda = 1.8$ is relatively multiform. In some regions, grains are elongated along the extrusion direction, with a width of 70–120 nm and a length of 220–550 nm. In other regions, equiaxed grains with a mean diameter of 130 nm are observed. The grain size and shape of RT-LSEM samples are similar to that of CT-LSEM samples. The inset shown in Fig. 7 is the selected area electron diffraction (SAED) pattern of each TEM micrograph. The SAED pattern of the RT-LSEM samples consists of discrete diffraction spots, indicating a refined structure and the misorientation angles between the subgrains formed in machining are generally smaller, while the SAED pattern of the CT-LSEM samples is distorted into discontinuous rings. In this case, an increase in high angle grain boundaries appears.

The heavily strained subgrains and elongated grains with diffused, nonequilibrium, and ill-defined boundaries are evident in both conditions shown in Fig. 7. However, a more severe deformed microstructure can be observed in the CT-LSEM samples due to the accumulation of dislocations. The dense dislocation cell structures are frequently shown in the CT-LSEM samples, while the microstructure of RT-LSEM samples is relatively "clean", and the dense dislocation areas decrease to a lower quantity as indicated in Figs. 7(b) and 7(d). In brief, CT promotes the formation and retention of high

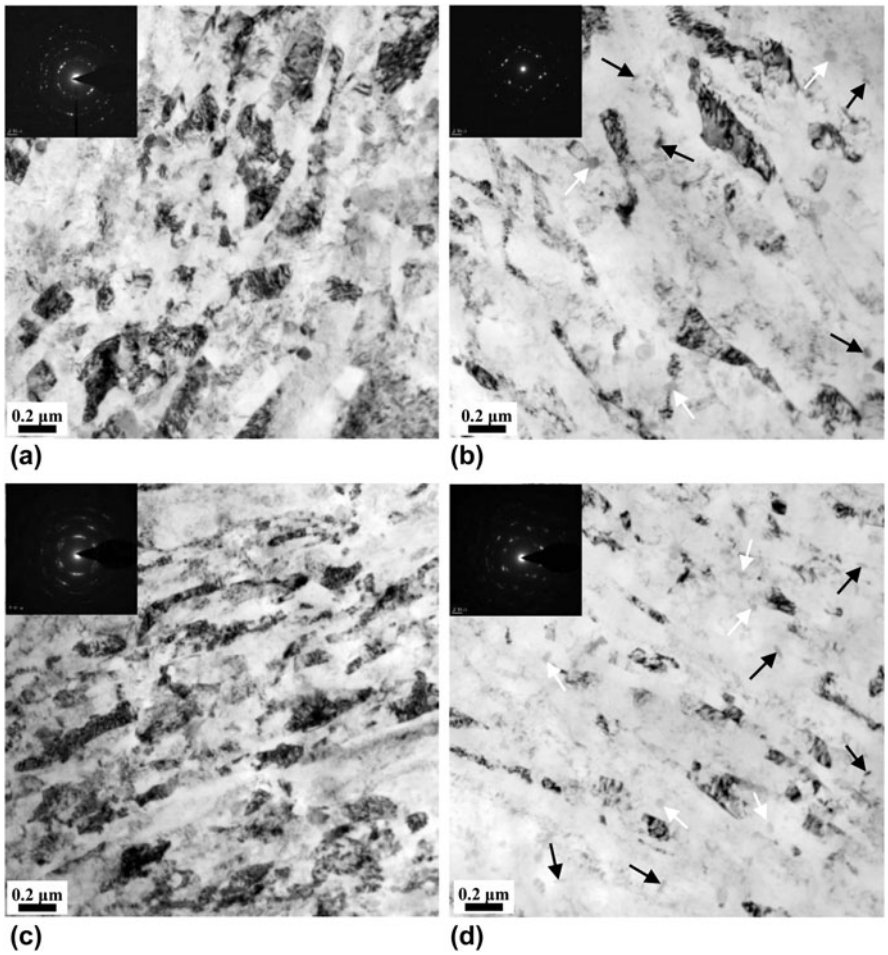


FIG. 7. TEM images and SAED patterns (insets) of the Al 7075 alloy subjected to (a) CT-LSEM and (b) RT-LSEM for $\lambda = 1.4$; (c) CT-LSEM and (d) RT-LSEM for $\lambda = 1.8$; the white-colored and the black-colored arrows in (b) and (d) represent η' and η precipitates, respectively.

https://doi.org/10.1557/jmr.2018.313 Published online by Cambridge University Press

density of defects, which also acts as driving forces for the formation of subgrains followed by ultrafine grains.

In RT-LSEM samples, dislocations are still observed within several well-defined subgrains. However, the dislocation density is sharply decreased compared with the CT-LSEM samples because when LSEM is implemented at RT, the generation of heat induced by friction and the plastic work inside the alloys activate the effective dynamic recovery and annihilation of dislocations. As dynamic recovery is mainly controlled by the dislocation climb and cross slip, temperature rising increases the dislocation movement and the rate of dynamic recovery, thus, resulting in annihilation of dislocations.[23–26]

However, it should be emphasized that a few needle-shaped and plate-shaped phases [marked by black-colored arrows and white-colored arrows in Figs. 7(b) and 7(d), respectively] are present in the RT-LSEM samples. Generally, the solute atoms in the ST Al 7075 such as Zn, Mg, Cu, Fe, and Mn are dissolved in the matrix. Since the Al 7075 alloy is a precipitation hardenable alloy, the precipitates are normally formed at the temperature range of 50–130 °C. During the RT-LSEM process, the chips are heated up to 100–170 °C which will trigger the precipitation behaviors inside the material. However, the metastable solutes failed to get sufficient thermal energy to precipitate out from solid solution during CT-LSEM. Since cryogenic deformation results in reduced solute diffusivity and therefore prevents strain-induced precipitation.[26] It can be deduced that the plate-shaped and needle-shaped phases are η' and η precipitates, respectively.[27]

In fact, precipitates are conductive to enhancing the hardness of alloys by pinning dislocations during deformation.[28] If these deformed alloys are further processed through heat-treatment optimization, large amounts of precipitates will then emerge out, and at the same time, the precipitation strengthening may dominate among the strengthening mechanisms which may be the focus of our future research.

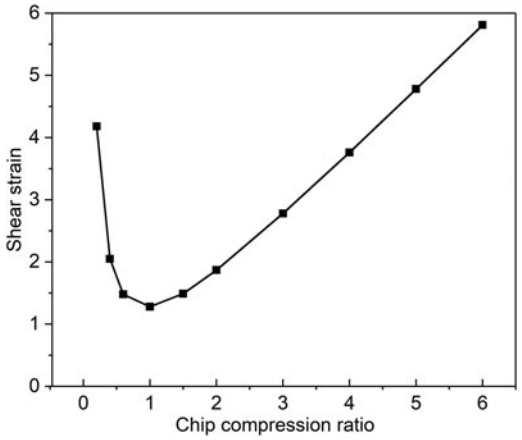


FIG. 8. Shear strains as a function of compression ratios for the rake angle of 20°.

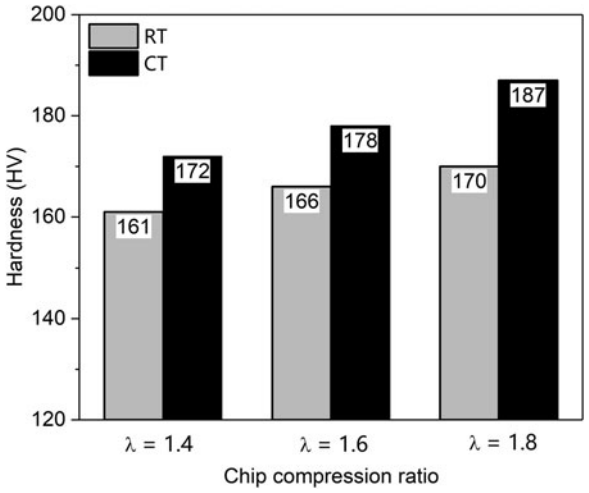


FIG. 9. Variations in hardness of the Al 7075 alloy processed by RT-LSEM and CT-LSEM for different compression ratios.

C. Hardness

Hardness is largely influenced by strains imposed on the materials during the machining process. Figure 8 shows the variation of ε with λ for the selected rake angle 20° [Eq. (1)]. This indicates that both reducing λ when $\lambda < 1$ and increasing λ when $\lambda > 1$ increase ε. For LSEM, the compression ratio λ is a reflection of the strain, when various strains can be achieved by altering λ. The effective strain corresponds to 1.43, 1.56, and 1.71 accordingly, when λ is 1.4, 1.6, and 1.8, respectively. Figure 9 shows the hardness variations of specimens as the function of λ for the rake angle of 20°. With reference to the hardness of the starting material (120HV), both methods exhibit high strengthening ability. It is noteworthy that the hardness increases with λ for the CT-LSEM and RT-LSEM specimens and the hardness of the former is higher than that of the latter for each λ. The hardness of the CT-LSEM specimen has increased significantly from 120 HV to 172 HV (43.3% increase), 178 HV (48.3% increase), and 187 HV (55.8% increase) for $\lambda = 1.4$, 1.6, and 1.8, respectively. As for the RT-LSEM specimens, the hardness increases linearly with λ and reaches the highest value of 170 HV for $\lambda = 1.8$, which is even 2 HV lower than the minimum hardness of the CT-LSEM specimens. Yu[28] has discovered the similar tendency in the hardness variation of Al 6××× subjected to cryo-rolling in their studies.

The improvement concerning the strength or hardness of Al alloys may be attributed to the following: (i) solid solution strengthening, (ii) precipitation strengthening, (iii) grain refinement strengthening, and (iv) dislocation

https://doi.org/10.1557/jmr.2018.313 Published online by Cambridge University Press

strengthening. In the present work, the workpiece is ST and quenched to obtain supersaturated solid solution materials owing to its higher work hardening rate and better microstructure refinement capabilities.[29] High solute content in the ST condition can increase the strength of the alloy by pinning the dislocations and impeding their motion during deformation. Clearly, solid strengthening operates in all conditions. The TEM micrographs indicate that there is a pronounced grain refinement in the ST alloys after being processed by LSEM. Grain refinement strengthening is generally described by the Hall–Patch equation in which the strength of materials is inversely proportional to the grain size. Here, the hardness version is used instead of the flow stress version:

$$H_V = H_0 + K_H d^{-1/2} \quad , \tag{5}$$

where H_V is the hardness; H_0 and K_H are the material constants; d is the average grain size of materials.[30] To examine the Hall–Patch relationship, the Vickers hardness values of the RT-LSEM and the CT-LSEM samples in Fig. 9 were plotted as a function of $d^{-1/2}$, which is shown in Fig. 10. This indicates that both the RT-LSEM and the CT-LSEM samples follow the linear relationship described by Eq. (5). Accordingly, grain refinement strengthening makes significant contribution to the hardness enhancement of all the samples subjected to LSEM.

The TEM micrographs reveal that high dislocation density exists in all conditions. The dislocations tangle together, forming dense dislocation cell structures and tangling zones and resulting in high dislocation density. The high density of dislocations decreases the mean free path of mobile dislocations, and the interactions among them hinder the dislocation slip and movement, thus causing the dislocation strengthening.[31] Hence, the dislocation strengthening is another critical factor that contributes to the hardness of the alloy. In high staking fault energy materials like aluminum, dynamic recovery is more active at RT, which causes reduction in strengthening effect by decreasing dislocation density. However, processing at CT inhibits dynamic recovery and causes dislocation accumulation for the higher-steady state level compared with RT processing. Therefore, the dislocation strengthening contribution is greater in the CT-LSEM samples than that in the RT-LSEM samples. The precipitation strengthening is based on the capacity of precipitates to retard dislocation motion. In this research, only few precipitates can precipitate out from the matrix during LSEM, accordingly, and the effect of precipitation strengthening is negligible.

Given all that, solid solution strengthening, grain refinement strengthening, and dislocation strengthening are the major strengthening mechanisms responsible for the hardness enhancement of the RT-LESM and CT-LSEM specimens. In particular, the dislocation strengthening contribution to the CT-LSEM samples overweighs that to the RT-LSEM samples, then resulting in higher hardness in the former.

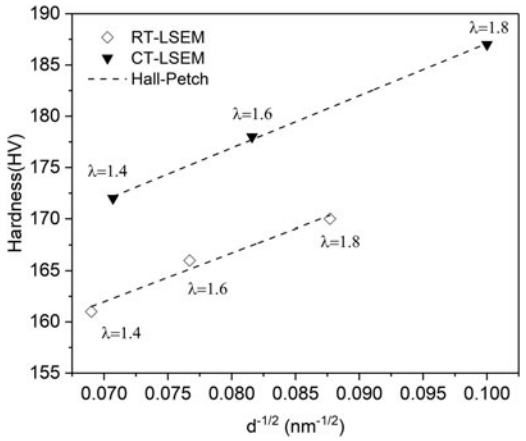


FIG. 10. Vickers hardness of samples processed by RT-LSEM and CT-LSEM as a function of $d^{-1/2}$.

IV. CONCLUSIONS

In this paper, cryogenic and RT LSEM was conducted with various compression ratios to investigate their comparative effects on chip morphology, microstructure, and hardness of UFG Al 7075 alloys. The main observations can be summarized in following conclusions:

(1) The chip morphology of CT-LSEM and RT-LSEM is significantly different, when the former is segmented and the latter is continuous due to the increased ductility of Al alloys at reduced temperature. CTs are conductive to improving the work-hardening capacity and the workability of the alloys.

(2) Grains in the bulk materials are refined to less than 200 nm via CT-LSEM, indicating that CT-LSEM is an operative approach for fabricating UFG materials. CTs suppress the dynamic recovery and therefore, lead to a complicated microstructure with high dislocation density.

(3) The hardness of the CT-LSEM and RT-LSEM samples increases with λ. Solution strengthening, grain refinement strengthening, and dislocation strengthening are responsible for the hardness enhancement. In particular, dislocation strengthening plays a more significant role in hardness enhancement of the CT-LSEM samples when compared with the RT-LSEM samples.

ACKNOWLEDGMENTS

This research was conducted under the support of the National Nature Science Foundation of China

https://doi.org/10.1557/jmr.2018.313 Published online by Cambridge University Press

(51375174), Fundamental Research Funds for Central Universities (2017ZD024), and Natural Science Foundation of Guangdong Province (S2013050014163 and 2017A030313260).

REFERENCES

1. M. Shamanian, H. Mostaan, M. Safari, and J.A. Szpunar: Friction stir modification of GTA 7075-T6 Al alloy weld joints: EBSD study and microstructural evolutions. *Arch. Civ. Mech. Eng.* **17**, 574 (2017).
2. W.S. Lee, W.C. Sue, C.F. Lin, and C.J. Wu: The strain rate and temperature dependence of the dynamic impact properties of 7075 aluminum alloy. *J. Mater. Process. Technol.* **100**, 116 (2000).
3. S.K. Panigrahi and R. Jayaganthan: Development of ultrafine grained high strength age hardenable al 7075 alloy by cryorolling. *Mater. Des.* **32**, 3150 (2011).
4. Y.H. Zhao, X.Z. Liao, Z. Jin, R.Z. Valiev, and Y.T. Zhu: Microstructures and mechanical properties of ultrafine grained 7075 al alloy processed by ECAP and their evolutions during annealing. *Acta Mater.* **52**, 4589 (2004).
5. S. Fritsch, M. Scholze, and M.F-X. Wanger: Cryogenic forming of AA7075 by equal-channel angular pressing. *Mater. Werkst.* **43**, 561 (2012).
6. W.J. Deng, W. Xia, C. Li, and Y. Tang: Formation of ultra-fine grained materials by machining and the characteristics of the deformation fields. *J. Mater. Process. Technol.* **209**, 4521 (2009).
7. Y.S. Li, N.R. Tao, and K. Lu: Microstructural evolution and nanostructure formation in copper during dynamic plastic deformation at cryogenic temperatures. *Acta Mater.* **56**, 230 (2008).
8. Y.H. Zhao, X.Z. Liao, S. Cheng, E. Ma, and Y.T. Zhu: Simultaneously increasing the ductility and strength of nanostructured alloys. *Adv. Mater.* **18**, 2280 (2006).
9. H.L. Yu, C. Lu, K. Tieu, H. Li, A. Godbole, X. Liu, and C. Kong: Enhanced materials performance of Al/Ti/Al laminate sheets subjected to cryogenic roll bonding. *J. Mater. Res.* **32**, 3761 (2017).
10. S. Swaminathan, M.R. Shankar, B.C. Rao, W.D. Compton, S. Chandrasekar, A.H. King, and K.H. Trumble: Severe plastic deformation (SPD) and nanostructured materials by machining. *J. Mater. Sci.* **42**, 1529 (2007).
11. W.J. Deng, Y.T. He, P. Lin, W. Xia, and Y. Tang: Investigation of the effect of rake angle on large strain extrusion machining. *Mater. Manuf. Processes* **29**, 621 (2014).
12. W.J. Deng, P. Lin, Z.C. Xie, and Q. Li: Analysis of large-strain extrusion machining with different chip compression ratios. *J. Nanomater.* **11**, 5271 (2012).
13. K. Palaniappan, H. Murthy, and B.C. Rao: Production of fine-grained foils by large strain extrusion-machining of textured Ti–6Al–4V. *J. Mater. Res.* **33**, 108 (2018).
14. P. Iglesias, M.D. Bermúdez, W. Moscoso, and S. Chandrasekar: Influence of processing parameters on wear resistance of nanostructured OFHC copper manufactured by large strain extrusion machining. *Wear* **268**, 178 (2010).
15. M. Efe, W. Moscoso, K.P. Trumble, W.D. Compton, and S. Chandrasekar: Mechanics of large strain extrusion machining and application to deformation processing of magnesium alloys. *Acta Mater.* **51**, 2031 (2012).
16. D. Umbrello, S. Caruso, and S. Imbrogno: Finite element modelling of microstructural changes in dry and cryogenic machining AISI 52100 steel. *Mater. Sci. Technol.* **32**, 1062 (2016).
17. S. Atlati, A. Moufki, M. Nouari, and B. Haddag: Interaction between the local tribological conditions at the tool–chip interface and the thermomechanical process in the primary shear zone when dry machining the aluminum alloy AA2024–T351. *Tribol. Int.* **105**, 326 (2017).
18. Y.B. Guo and D.W. Yen: A FEM study on mechanisms of discontinuous chip formation in hard machining. *J. Mater. Process. Technol.* **155–156**, 1350 (2004).
19. C. Ye, S. Suslov, D. Lin, and Y. Liao: Cryogenic ultrahigh strain rate deformation induced hybrid nanotwinned microstructure for high strength and high ductility. *J. Appl. Phys.* **115**, 213519 (2014).
20. D.H. Park, S.W. Choi, J.H. Kim, and J.M. Lee: Cryogenic mechanical behavior of 5000- and 6000-series aluminum alloys: Issues on application to offshore plants. *Cryogenics* **68**, 44 (2015).
21. W. Moscoso, M.R. Shankar, J.B. Mann, W.D. Compton, and S. Chandrasekar: Bulk nanostructured materials by large strain extrusion machining. *J. Mater. Res.* **22**, 201 (2007).
22. Z. Pu, J.C. Outeiro, and A.C. Batista: Enhanced surface integrity of AZ31B Mg alloy by cryogenic machining towards improved functional performance of machined components. *Int. J. Mach. Tool Manufact.* **56**, 17 (2012).
23. M. Abbasi-Baharanchi, F. Karimzadeh, and M.H. Enayati: Mechanical and tribological behavior of severely plastic deformed Al6061 at cryogenic temperatures. *Mater. Sci. Eng., A* **683**, 56 (2017).
24. D.C.C. Magalhães, A.M. Kliauga, M. Ferrante, and V.L. Sordi: Plastic deformation of FCC alloys at cryogenic temperature: The effect of stacking-fault energy on microstructure and tensile behaviour. *J. Mater. Sci.* **52**, 7466 (2017).
25. Y. Wang, T. Jiao, and E. Ma: Dynamic processes for nanostructure development in Cu after severe cryogenic rolling deformation. *Mater. Trans.* **44**, 1926 (2005).
26. V.S. Sarma, W.W. Jian, J. Wang, H. Conrad, and Y.T. Zhu: Effect of rolling temperature on the evolution of defects and properties of an Al–Cu alloy. *J. Mater. Sci.* **45**, 4846 (2010).
27. S.K. Panigrahi and R. Jayaganthan: Effect of annealing on thermal stability, precipitate evolution, and mechanical properties of cryorolled Al 7075 alloy. *Metall. Mater. Trans. A* **42**, 3208 (2011).
28. H.L. Yu, A.K. Tieu, C. Lu, X.H. Liu, A. Godbole, and C. Kong: Mechanical properties of Al–Mg–Si alloy sheets produced using asymmetric cryorolling and ageing treatment. *Mater. Sci. Eng., A* **568**, 212 (2013).
29. S.K. Panigrahi and R. Jayaganthan: Development of ultrafine-grained Al 6063 alloy by cryorolling with the optimized initial heat treatment conditions. *Mater. Des.* **32**, 2172 (2011).
30. W.J. Kim and Y.K. Sa: Micro-extrusion of ECAP processed magnesium alloy for production of high strength magnesium micro-gears. *Scr. Mater.* **54**, 1391 (2006).
31. P.N. Rao, D. Singh, H.G. Brokmeier, and R. Jayaganthan: Effect of ageing on tensile behavior of ultrafine grained Al 6061 alloy. *Mater. Sci. Eng., A* **641**, 391 (2015).

https://doi.org/10.1557/jmr.2018.313 Published online by Cambridge University Press